FULL RESEARCH ARTICLE

A comparative study of the mechanical characteristics of additively and conventionally fabricated 17-4 precipitation hardened stainless steel

Hamid Eisazadeh[1] · Sandeep Khadka[2] · Xiaoqing Wang[3,4] · Philip Yuya[2]

Abstract

Precipitation hardened stainless steel, like 17-4PH SS, had received significant interest in various industries due to its high strength and corrosion resistance properties. This material may be produced with either traditional or modern manufacturing techniques. However, each carries its benefits and challenges. In this study, 17-4 PH parts produced by laser powder bed fusion (L-PBF) and traditional manufacturing (wrought) techniques are characterized by different method like a tensile test, microhardness, and nanoindentation. The primary aim of this research is to examine the impact of heat treatment on the properties of 17-4PH, comparing specimens manufactured through L-PBF and conventional manufacturing methods. The investigation seeks to determine whether the heat treatment induces similar magnitude changes in both sets of parts, with an emphasis on utilizing a diverse range of characterization techniques for comprehensive analysis. Solution annealing followed by an aging process was employed to investigate post-heat treatment's impact on the performance of 17–4 PH SS parts in both manufactured parts. Results showed that modulus and hardness of L-PBF additive manufacturing parts were lower than those of conventionally manufactured counterparts. Solution annealing and aging increased these properties significantly in both cases; however, both ductility and ultimate strength of 17-4 PH stainless steel parts produced via the additive manufacturing are still inferior compared to their wrought parts.

Keywords 17-4 PH precipitation hardened stainless steel · Nanoindentation · Laser powder bed fusion (L-PBF) · Solution annealing · Aging treatment · Martensitic steel

1 Introduction

Powder Bed Fusion (PBF) represents a prominent technique in additive manufacturing (AM), aimed at fabricating intricate and lightweight components directly from computer-aided design (CAD) data. This sophisticated technology employs a heat source with focused density, such as a laser beam, to selectively melt and fuse metallic powders with diameters ranging from 10 to 60 μm in a layer-by-layer manner [1]. Nevertheless, challenges persist in achieving optimized properties, including microstructural and mechanical attributes, in PBF-manufactured parts comparable to those produced using conventional manufacturing techniques [2–4]. These challenges stem from the significant thermal gradients formed within the parts during the rapid melting and solidification processes of PBF [5]. The utilization of intense heating and cooling cycles during the AM process leads to various defects within the parts [6]. These defects encompass porosity, entrapped vapor voids, residual stresses, unidirectional grain growth, micro-segregation of solute elements, as well as the presence of non-equilibrium phases. These defects subsequently exert a detrimental influence on critical mechanical properties like Young's modulus and hardness [7].

The complex microstructural development in AM is governed by a multitude of factors, including scanning patterns,

✉ Hamid Eisazadeh
  heisazad@odu.edu

1 Engineering Technology Department, Old Dominion University, Norfolk, VA 23529, USA

2 Mechanical & Aerospace Engineering Department, Clarkson University, Potsdam, NY 13699, USA

3 Department of Applied Engineering, Jacksonville State University, Jacksonville, AL 36265, USA

4 Present Address: Central Engineering, Kulicke and Soffa Industries, Fort Washington, PA 19034, USA

laser beam parameters, build chamber conditions, and many machine related variables [8–10]. Understanding and optimizing these factors hold significant potential for advancing AM technology and its applications in diverse industries. For instance, experimental studies by Chery et al. and Burkhardt et al. have demonstrated that lowering the laser energy intensity below its optimal threshold may result in a larger amount of porosity and reduced hardness of AM 304/316 stainless steel components[11, 12]. In contrast, excessively high-laser energy density can induce balling defects, leading to the formation of unmelted regions [13]. The microstructure of AM parts can be significantly affected by the beam scan strategy. For example, an island scan strategy, which results in the powder being melted in isolated islands, can produce a bi-modal grain structure, with a mixture of fine and coarse grains [9]. In contrast, a back-and-forth scan strategy, which results in the powder being melted in a continuous line, can produce a columnar grain structure, with elongated grains that are oriented in the build direction. The reduction of porosity and unmelted powder in AM components can be achieved by selecting appropriate powder and adjusting machine settings [14, 15]. However, despite these efforts, the inherent rapid heating, melting, solidification, and recrystallization processes in AM still lead to microstructural heterogeneities and anisotropy in nearly all instances. Currently, these effects are mitigated to some extent by post-processing operations [16]. Heat treatments, one of these operations, are utilized to relieve residual stresses and promote microstructure uniformity. Thereby, they yield microstructural characteristics comparable to those typically obtained through conventional manufacturing, such as forging and casting.

Over the past decade, the laser assisted PBF (L-PBT) method has enabled the production of various steel types, with increasing attention being directed toward precipitation hardened (PH) stainless steel due to its unique martensitic/austenitic microstructure [17–19]. Notably, 17-4PH, one of these alloys, has found widespread utility across diverse fields, owing to its highly desirable mechanical properties encompassing strength, corrosion resistance, and hardness. Generally, the strength improvement observed in the 17-4PH alloy arises from the precipitation of finely dispersed nanoscale particles rich in copper (Cu) [20–22]. Consequently, post-processing heat treatments become imperative. The requirement for post-processing emerges as a result of the non-equilibrium microstructure found in as-built 17-4PH parts, exhibiting a distinct texture aligned parallel to the build direction [23]. These microstructural characteristics significantly influence the mechanical properties of AM parts when compared to their conventionally manufactured counterparts [24–28]. For instance, the non-equilibrium solidification and build chamber conditions used in AM can result in incomplete transformation from austenite to martensite, resulting in a larger fraction of retained austenite in

the final product [21, 25]. This is because nitrogen, which is a common atmosphere provided in the build chamber, stabilizes the austenite phase. In a research conducted by Rafi et al. [21], it was observed that the amount of austenite in 17-4PH AM parts fabricated with an argon atmosphere was approximately 8 vol.%. In contrast, for 17-4PH parts produced under a nitrogen atmosphere, the volume fraction of austenite was found to be around 65 vol.%. The presence of retained austenite is a critical factor influencing the properties of 17-4PH, impacting characteristics such as strength and toughness [29]. A study by Kudzal et al. has reported that L-PBF parts made of 17-4PH may exhibit reduced ductility attributable to the amount of retained austenite and other imperfections arising from additive layering strategies [30]. It is noteworthy that wrought 17-4PH materials, in contrast to AM parts, typically demonstrate microstructures predominantly composed of martensite, along with the presence of finely dispersed precipitates rich in Cu.

Several investigations have been conducted on post-processing techniques aimed at altering the fractions of microstructure phases, and particularly addressing heterogeneous grain morphology in 17-4PH AM parts [26]. For example, LeBrun et al. [31] explored the influence of varying temperature and time during heat treatment on the mechanical properties. Cheruvathur et al. [32] also studied the application of heat treatments to achieve uniform microstructures in AM 17-4PH materials. They discovered that subjecting the material to solution annealing above 1100 °C resulted in the effective elimination of the dendritic-solidification structure. Furthermore, in the heat-treated condition, it induced a significant reduction in the proportion of retained austenite, decreasing from 50% observed in the as-built condition to 10%. Despite these improvements, the heat-treated parts yet displayed heterogenous microstructures. Bai's study [33] indicated that the utilization of solution annealing or a combination of solution annealing and aging treatments after the build process has potential to mitigate the concentration of undesirable microstructures, such as solute segregation. The investigation further revealed that the application of the solution treatment resulted in a decrease in microhardness and tensile strength, accompanied by an increase in elongation. Conversely, after aging treatment, both microhardness and tensile strength exhibited significant enhancement, while elongation experienced a reduction.

Despite growing attention in use of 17-4 PH steel via L-PBT, comparative macro, micro, and nano-scale properties between AM and conventional manufactured parts remains limited in the existing literature. The recent study by Roberts et al. [28], for instance, initiated a preliminary investigation on microstructural characteristics, microhardness, and high-temperature mechanical property data of 15-5 PH SS in comparison to the traditionally manufactured. As such, addressing this research gap is valuable for advancing

the field of AM 17-4 PH steel and elucidating the potential benefits and limitations of utilizing L-BPT for producing components with comparable mechanical properties to their conventionally manufactured counterparts. Nano-scale properties of AM parts can directly be achieved through nanoindentation which is a non-destructive technique. This method provides in-situ indentation measurements at the micro-/nanoscale on a small area for various materials. Thus, it has been widely utilized to probe the mechanical behavior of AM alloys [34–38]. The comparison studies between conventional and additively manufactured 17-4 PH stainless steels have been done in the past [39–41]. However, none of the published work, compared reduced modulus, nanohardness, and load–displacement curves of AM-processed 17-4 PH with their counterparts manufactured through conventional technologies like casting and forging processes. The primary objective is to comprehend whether solution annealing + aging treatment can modify the properties of 17-4PH to the same extent whether it is made by L-PBT or wrought using various characterization tools. As such, an investigation on the comparison of microstructure, nanoindentation results, micro hardness, and tensile strength of AM and conventional manufactured parts with and without solution annealing + aging treatment was carried out in this study. This research provides an additional understanding of the 17-4 PH stainless steel parts fabricated via L-PBF process.

2 Materials and methods

The 17-4 PH stainless steel powder used in the study was obtained from EOS GmbH [42]. This powder exhibited a particle size distribution with a D50 value ranging from 36 to 44 μm. The powder was produced through the gas-atomization technique, resulting in a spherical morphology as shown in the SEM image in Fig. 1. Larger particles display a more distinct and well-defined arrangement, with increased separation between them. Conversely, finer particles tend to aggregate together in clusters due to the stronger adhesive forces acting between them, which become more significant compared to the gravitational forces (their weight). The platform temperature was set to 100 °C. Chemical composition of the 17-4 PH stainless steel powder is provided in Table 1.

Tensile testing coupons were fabricated horizontally (XY orientation) using an ORLAS Creator machine. The specimens were laid out level on the build plate and parallel to the powder spreading direction. The coupons had a gage section, width, and thickness of 32 mm, 6 mm, and 3.175 mm, respectively (see Fig. 2). Tensile tests were performed at a strain rate of 1 mm/min according to the ASTM E466 standard.

The PBF process parameters like the speed of scanning, hatch distance, power, and thickness of layers are provided
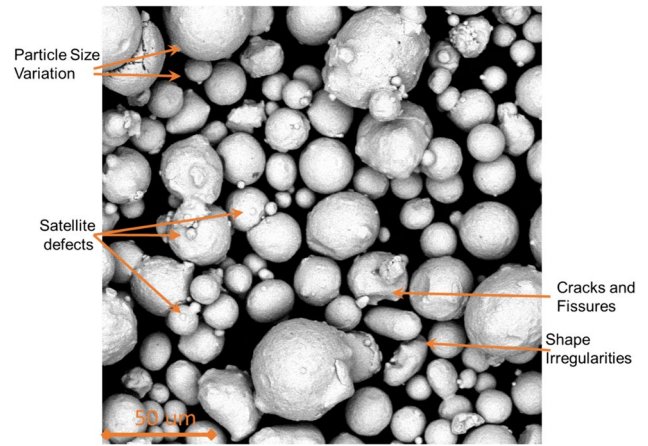

Fig. 1 SEM image depicting the as-received 17-4 PH stainless steel powder along with various observed defects

in Table 2. These are the optimized processing setting for the printing 17-4PH that were recommended by the ORLAS Creator machine manufacturer. The choice of hatch strategy has a significant impact on the microstructure and morphology of grains in L-PBF parts. In this study, a simple back-and-forth hatch strategy with a shifting angle of 45° was employed, in accordance with the manufacturer's recommendations for building tensile test parts. However, no support structures were used, as the manufacturer does not recommend their use for this application. These variables can be studied in future studies.

2.1 Heat treatment parameters

Generally, the mechanical properties of as-built's L-PBF parts do not meet the ASM standard for in-service performance unless post-heat treatment is carried out to enhance the microstructure of AM 17-4 PH SS parts [43, 44]. This is mainly because these SLM parts do not form entirely martensite microstructure in as-built condition. This is typically due to the high-thermal gradient and solidification rate during the SLM process that facilitate production of metastable austenite microstructure and prevent formation of martensite phase. Higher fraction of retained austenite phase affect the tensile strength of material, hardening, and elongation before failure [25, 45]. In this study, both wrought and L-PBT parts underwent post-process heat treatment, which involved three steps: solution annealing, air cooling, and aging. Direct aging of as-built 17-4 PH parts does not result in age-hardening due to the dual-phase microstructure of martensite and austenite [25, 46]. Therefore, both solution annealing and aging were utilized in this study to investigate the effects of these heat treatments on the microstructure of L-PBT and wrought parts. Six wrought and as-built SLM parts underwent solution annealing by heating

Table 1 Chemical composition of the 17-4 PH stainless steel powder (wt-%), wrought, and SLM

	Fe	Cr	Ni	Cu	Si	Mn	C	P	S	Nb + Ta
Powder	Bal	16.2	4.2	3.8	0.38	0.46	0–0.07	0–0.02	0–0.03	0.35
Wrought	Bal	14.3	3.56	2.86	0.36	0.44	0–0.07	0.028	0.02	0.22
SLM	Bal	15.3	3.7	3.3	0.81	0.48	0–0.07	0.017	0.027	0.25
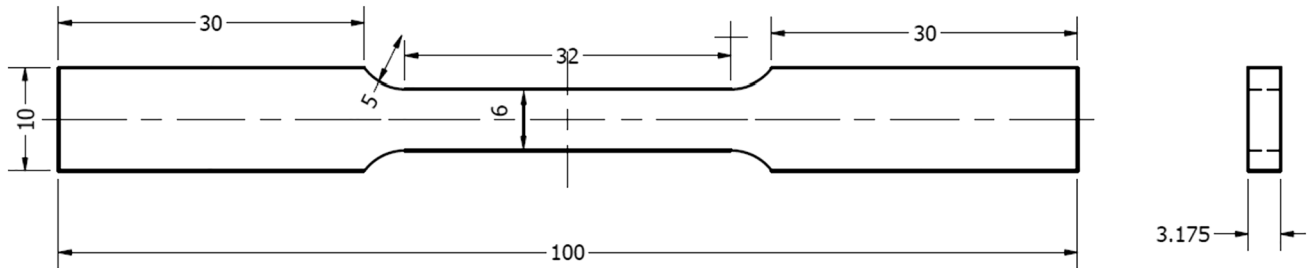
Fig. 2 Dimension of tensile test specimen according to ASTM E466 standard

Table 2 SLM processing settings for 17-4 PH samples

Machine	Type of laser	Power, Watt	Thickness of layers, μm	Hatch spacing, μm	Speed of scanning, mm/s	Spot size, um	Overlap, %	Hatch strategy
ORLAS Creator	Yb Fiber	107.3	25	50	1200	50	80	Back and forth with a shifting angle of 45

to approximately 1040 °C for 30 min, followed by slow air cooling. Subsequently, the samples were precipitation hardened at 460 °C for 1 h, and finally, they were air-cooled to room temperature.

2.2 Tensile test

Tensile tests were conducted in accordance with ASTM E466 using a strain rate of 1 mm/min on the MTS Landmark Servo-hydraulic Test System. Three replications were performed to ensure the reliability of the results. The dimensions of the specimens are shown in Fig. 2.

2.3 Microstructure

The specimens for microstructure examination and microhardness study were prepared using standard metallographic procedures. The specimens were sectioned into smaller pieces using a high-speed cutting machine. Subsequently, these pieces were mounted in epoxy to expose their cross-sections for grinding and polishing. Surface grinding was executed using SiC papers of various grit sizes, ranging from 80 to 320, followed by surface polishing with grit sizes from 400 to 1200. The attainment of

a mirror-finish surface was achieved through the use of alumina suspension with grit sizes of 1, 0.5, and 0.3 μm. Finally, the samples were polished using a vibratory polisher with 50 nm colloidal silica. Microstructure and phase constituents studies were performed using scanning electron microscope (SEM), electron backscatter diffraction (EBSD), and X-ray diffraction (XRD). An Electron Backscattered Diffraction (EBSD) Oxford Instruments C-Nano equipped in JEOL JSM 7900F SEM along with an Oxford Instruments Aztec Ultim Max 65 mm^2 EDS detector was used to analyze the sample's microstructure, chemical composition, phase content, grain size, and orientation. EBSD was operated at 20 kV, with a step size of 0.018 μm, and analyzed using Oxford Instruments Aztec and Aztec Crystal software packages and database. A Malvern X′Pert Pro MRD X-Ray Diffractometer in the Bragg–Brentano geometry using Cu-Kα X-ray was operated at 40 mA and 45 kV scanning from $2\theta = 30$–100° at a step size of 0.02° for phase analysis. Microhardness assessment was conducted utilizing a Vickers hardness indenter with a 500 gf load and a 10-s dwell time. The individual specimen's microhardness was determined by considering the average value obtained from five tests conducted at distinct locations.

2.4 Nanoindentation

Nanoindentation mapping was carried out using the Triboindenter 950, a nanoindentation instrument (Bruker Co., Billerica, MA, USA), on the polished surfaces of the samples to acquire comprehensive data on local mechanical properties, including hardness and elastic modulus. In this study, a standard diamond Berkovich tip with a three-faceted pyramid, featuring total and half angles of 142.3 ° and 65.35 °, respectively, along with a curvature radius of 150 nm, was utilized (as shown in Fig. 3). Indentations were performed using a standard, quasi-static trapezoidal loading function, employing a load-controlled series of indents in which the tip was brought into contact with the specimen in a direction perpendicular to the build plane. The load-controlled module applied a peak load of 7000 μN, with each indent being held for 2 s. To mitigate influence of surface roughness on nanoindentation measurements, samples were polished to a surface roughness of approximately 50 nm. This process utilized dry and wet polishing. Coarse grit-like 300 grit papers to 50 nm colloidal silica on a vibratory polisher were used to create a mirrored finish on the sample surface. In addition, by defining at least 10 microns of space between the indents in the indent location grid, it was assured that the indents did not interface with each other.

Oliver-Pharr method uses the load–displacement data to the hardness (H) and reduced or nanoindentation modulus (E_r). Stiffness values from 95 to 20 % of the initial unloading curves were determined by fitting this information to contact mechanical theory for an isotropic, elastic half-space for each individual curve. The reduced modulus d was
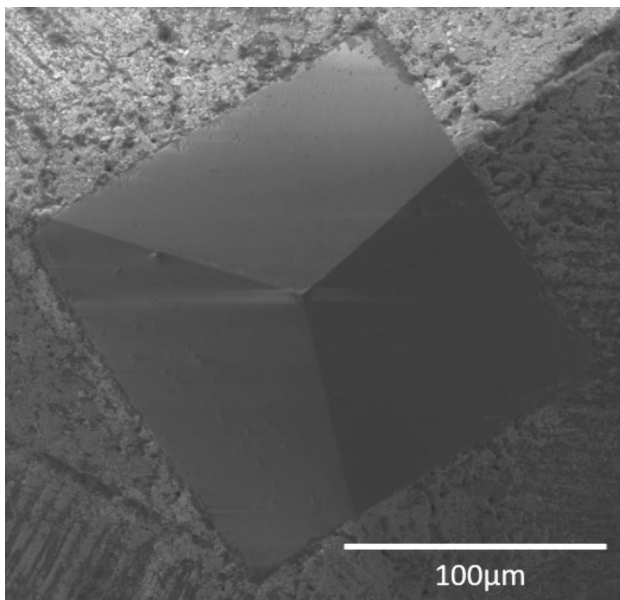

Fig. 3 A SEM image of diamond Berkovich tip used in this study

determined from the composite modulus given by: $[\frac{1-v^2}{E} + \frac{1-v_i^2}{E_i}]^{-1}$ where v_i and E_i are the Poisson's ratio and Young's modulus of the indenter tip, which are 0.07, 1140 GPa, respectively for a diamond Berkovich indenter. The hardness (H), expressed as $H = \frac{P_{max}}{A}$, is the ratio of the maximum force to the contact area A, which is determined from a calibrated tip area.

3 Results and discussion

3.1 Tensile performance

Figure 4 presents the outcomes of tensile tests conducted on both heat-treated and as-built L-PBF and wrought specimens. The results indicated that the tensile strength of the as-built L-PBF parts (731 MPa) was significantly lower than that of all other specimens, thereby revealing insufficient mechanical properties for their application as functional parts for end-users with as-built condition. The as-built L-PBF part usually exhibit lower tensile strength compared to those of the wrought sample, which is accordance to ASTM A693 due to heterogeneous microstructure and residual stresses.

Table 3 shows that both L-PBF and wrought specimens experienced increased ultimate tensile strength after solution annealing + aging by reducing the retained austenite (discussed further in the microstructure section). Notably, the yield strength of as-built L-PBF parts was the lowest, while its heat-treated parts became comparable to those of heat-treated wrought specimens.

Table 3 also illustrates that the elongation reduced significantly for the L-PBF sample after solution annealing + aging. Elongations to failure for the as-built specimen is 10.9%, which is much higher than that of the heat-treated specimen 7.6%. This inverse relation between yield strength and elongation or ductility was observed by prior studies [22, 47]. Previous research, such as that by Nezhadfar et al. [47] demonstrated a similar effect of precipitation hardening heat treatment (e.g., H900) on both wrought and L-PBF 17-4PH stainless steel, increasing yield and tensile strength while decreasing ductility due to Cu-rich precipitates.

In the heat treatment process (solution annealing + aging) of 17-4 PH steel, austenite formation is minimized or eliminated. However, by increasing the aging temperature or aging time, ductility can be improved, with a significant loss of tensile strength. This is because longer aging times and higher temperatures cause precipitates to coarsen and reduce their coherency with the matrix. Coherent precipitates are essential for maintaining strength, so when they coarsen, the strength of the material decreases [6].

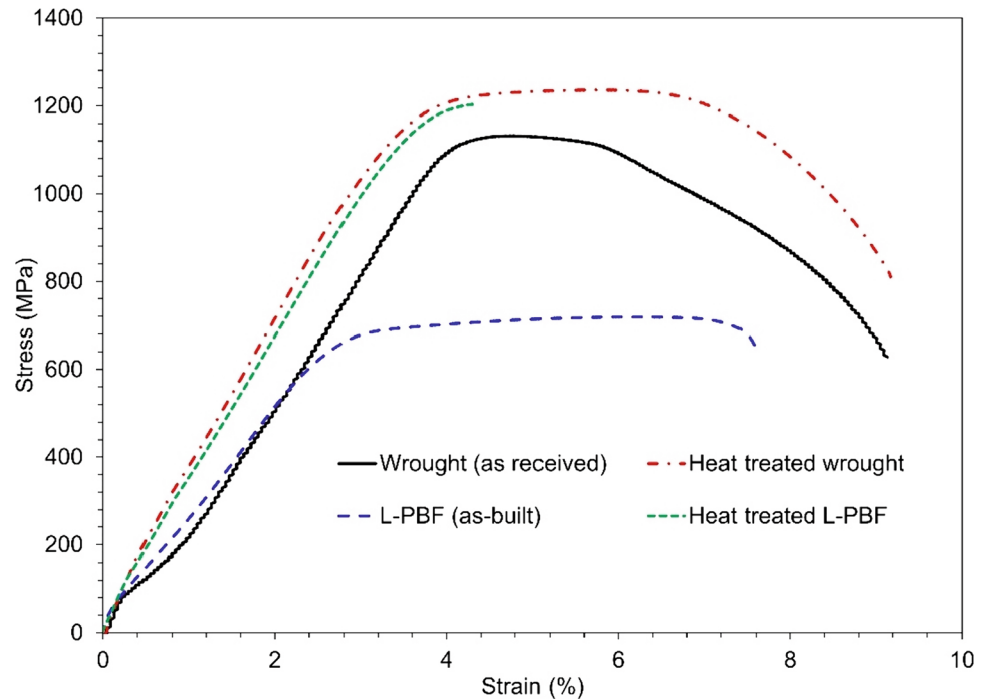**Fig. 4** Strain–stress curves obtained from tensile tests of 17-4 PH SS samples prepared through four different conditions

Table 3 Summary of tensile test results of wrought and L-PBF specimens with/without heat treatments

Materials	Preparation method	Yield stress, MPa (STDEV)	Ultimate tensile stress, MPa (STDEV)	Elongation to failure, % (STDEV)
Wrought	As received	1093 (15)	1124 (10)	13.7 (2)
	Heat treated	1166 (67)	1244 (21)	12.7 (2.2)
L-PBF	As built	687 (74)	731 (38)	10.9 (0.8)
	Heat treated	1124 (17)	1198 (8)	7.6 (1.5)

The high ductility of L-PBF parts under as-built condition may be due to various AM imperfections like unmelted powder and porosity. Porosity is the presence of voids or holes in the material, resulting from entrapped gas and lack of fusion in AM process. Generally, it increases the ductility of L-PBF parts, while reducing their strength [48]. In addition, the as-built microstructure of 17-4PH produced by L-PBF is typically a mixture of martensite and austenite. Although martensite is a hard and brittle phase, austenite is a soft and ductile phase and its presence gives L-PBT part greater ductility [49].

3.2 Microstructure characterization

Figure 5 shows the XRD patterns of the wrought and L-PBF 17-4 PH steel including the heat-treated samples. As seen from the figure, the alloy forms predominantly martensite phase in the microstructure along with minor amount of austenite phase. The combination of martensite and austenite phase has been noted and studied in various other wrought and L-PBF 17-4 PH steel along with their heat-treated counterpart [25, 36, 50–52]. The phase composition of 17-4 PH steel cannot be unequivocally guaranteed based on the spectra analysis of XRD. The unique nature of martensite in 17-4 steel exhibits crystal structure very similar to the body centric cubic structure (BCC) of ferrites. The challenges and complicated process of correctly identifying the phase constituents in the 17-4 PH steel has resulted in various studies looking into the comprehensive examination of the microstructure images on distinctively identifying martensite and austenite phases in the alloy [36, 50, 51, 53]. The chemical composition of Ni/Cr in the alloy has been noted to affect the martensite-formation tendency in the 17-4 PH steel [50–52]. For the composition of high Cr/Ni ratio, the rapid rates of heating and cooling hinder the formation of austenite, preventing the transformation of initial delta ferrite. Conversely, a low-Cr/Ni ratio permits the transformation of delta ferrite to austenite, and during the subsequent cooling phase, the formed austenite evolves into martensite[50–52].
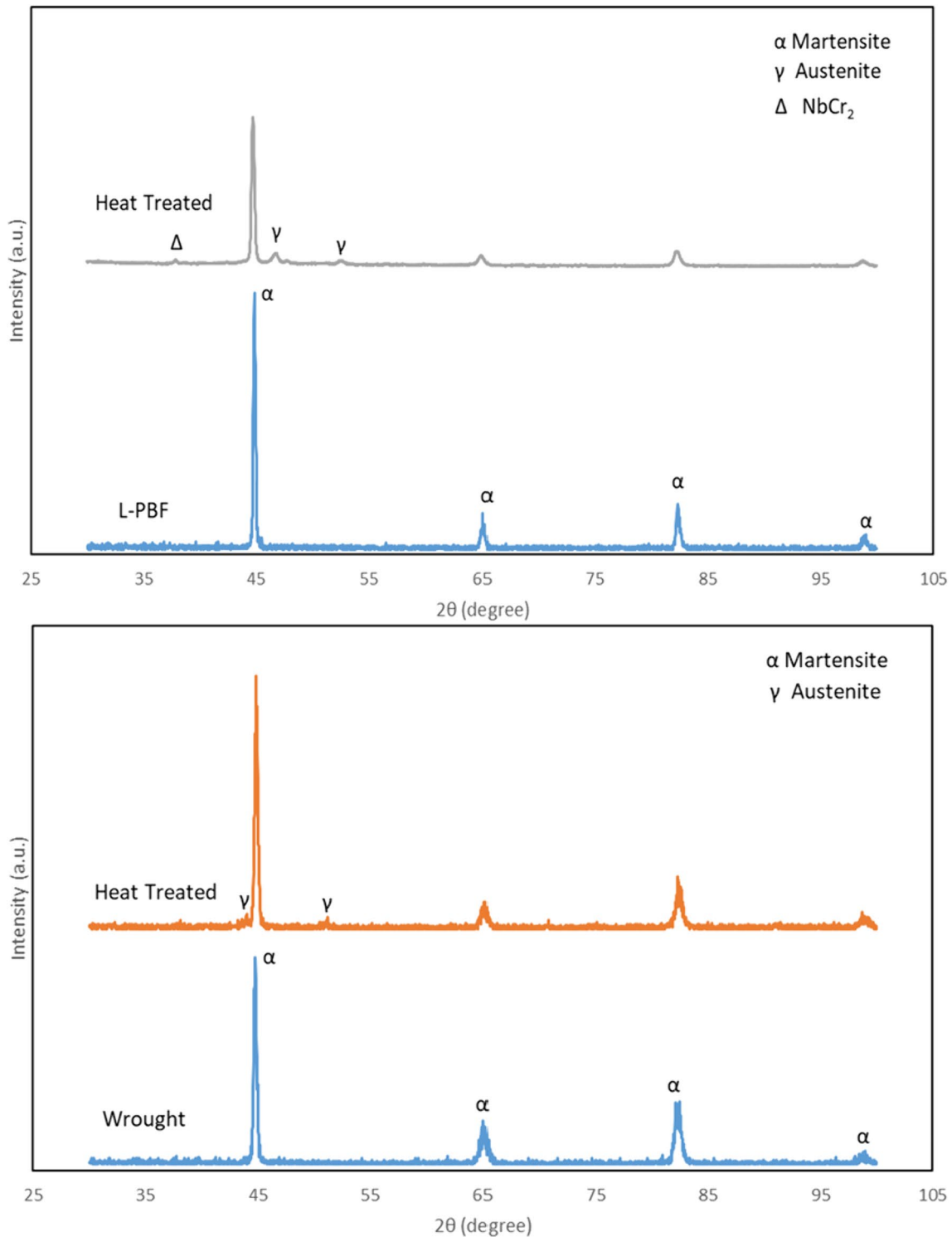
Fig. 5 XRD spectra of wrought and L-PBF 17-4 PH steel along with heat-treated samples

Furthermore, the gasses present during the additive manufacturing process has been shown to encourage the formation of austenite which is then transformed into martensite during the rapid solidification cooling [36, 51, 53].

Figure 6 shows the microstructure of the wrought and L-PBF 17-4 PH steel along with the microstructure of the heat-treated wrought and L-PBF samples. The presence of martensite, austenite, and precipitates are highlighted in
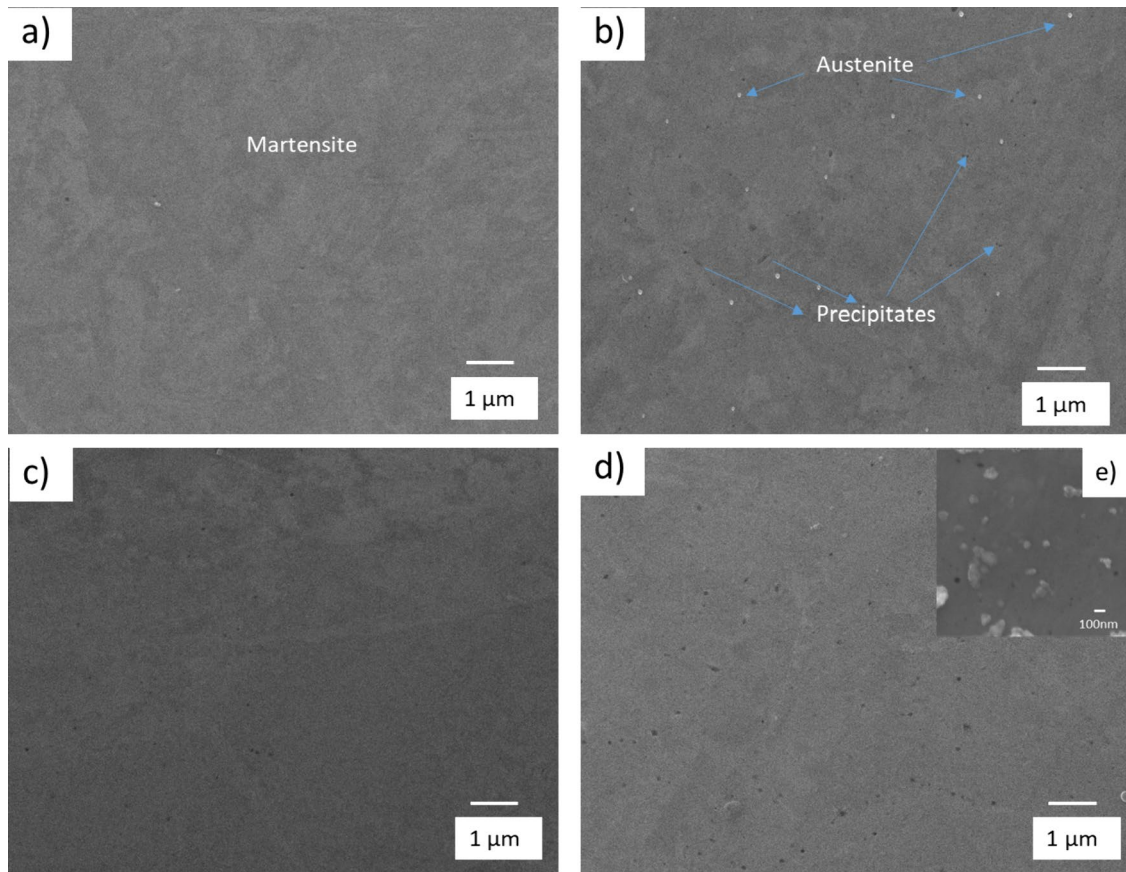
Fig. 6 Microstructure of the samples: (**a**) Wrought, (**b**) Wrought treated, (**c**) L-PBF, (**d**) L-PBF treated, (**e**) inset showing cluster of austenite and precipitates

the figure. Furthermore, Fig. 6(e) shows the cluster of the austenite and precipitates present in the microstructure. The martensite present in the alloy as identified in the XRD spectra is indicative of α-Fe (BCC, $a = 0.286$ nm) while the austenite is indicative of γ-austenite (FCC, $a = 0.385$ nm). In addition, trace amount of $NbCr_2$ was identified in the XRD spectra. The composition of $NbCr_2$ as a precipitates formed in the 17-4 PH steel has been noted in various studies [51, 52]. Finally, the confirmation of martensite being the dominant phase in room temperature was confirmed by the subsequent hardness measurements.

EBSD analysis was employed to examine the crystallography of the samples. The texture of the grains, grain orientation and grain-size distribution of wrought and L-PBF 17-4 PH steels has been studied. Also, the influence of heat treatment on the microstructural characteristics inherent to both wrought and AM parts has also been studied. Cross-sectional slices were meticulously obtained from the specimens, aligning perpendicular with the build direction. Grain-orientation maps were constructed, with visual representations provided in Figs. 7, 8, 9, 10.

EBSD analysis confirms that the fully martensitic structure as observed in Fig. 6(a) of the wrought parts are indeed fully martensitic while the heat-treated parts as observed in Fig. 6(b) has austenite grains. The average grain size is 5.4 μm in as-built condition and it reduces to 3.69 μm after heat treatment while the percentage of austenite phase after heat treatment is seen to be slightly higher at 0.2%. L-PBF parts under as-built condition reveals similar transformation sequence as wrought parts. The grain size of the L-PBF samples reduced to an average of 34.37 μm from 48.63 μm after heat treatment and the percentage of austenite showed minor increase of just 0.1%. Initially, very small amount of austenite are observed in the L-PBF as-built sample which is observed to the nature of L-PBF process which could result in trace amount of austenite trapped in the microstructure which are affected by the laser scanning paths [25, 36, 51, 52]. During heat treatment process, the reversion of austenite takes place due to the diffusion between the elements present in the alloy causing chemical stabilization. Subsequently, the austenite is reversed into martensite during the post treatment cooling phase, the result of the treatment
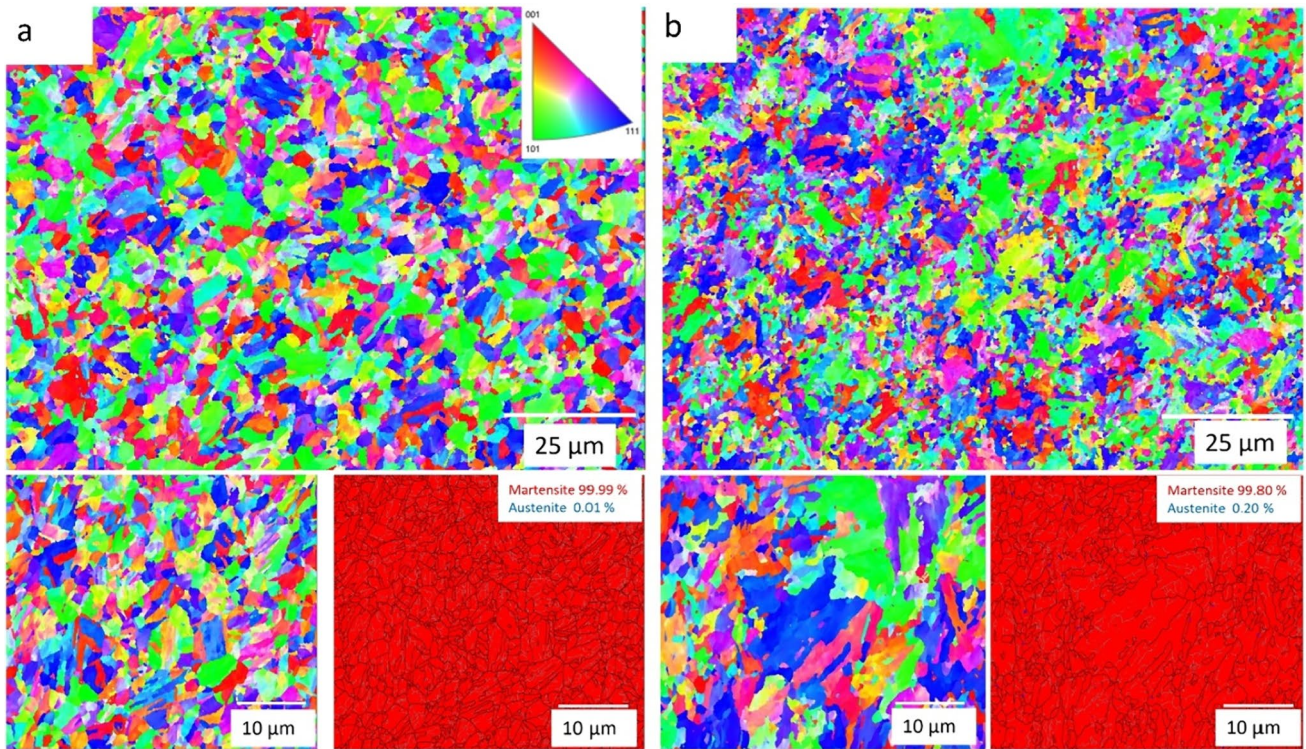
Fig. 7 EBSD orientation maps obtained from wrought parts along perpendicular to build direction: (**a**) as-received, (**b**) heat-treated part
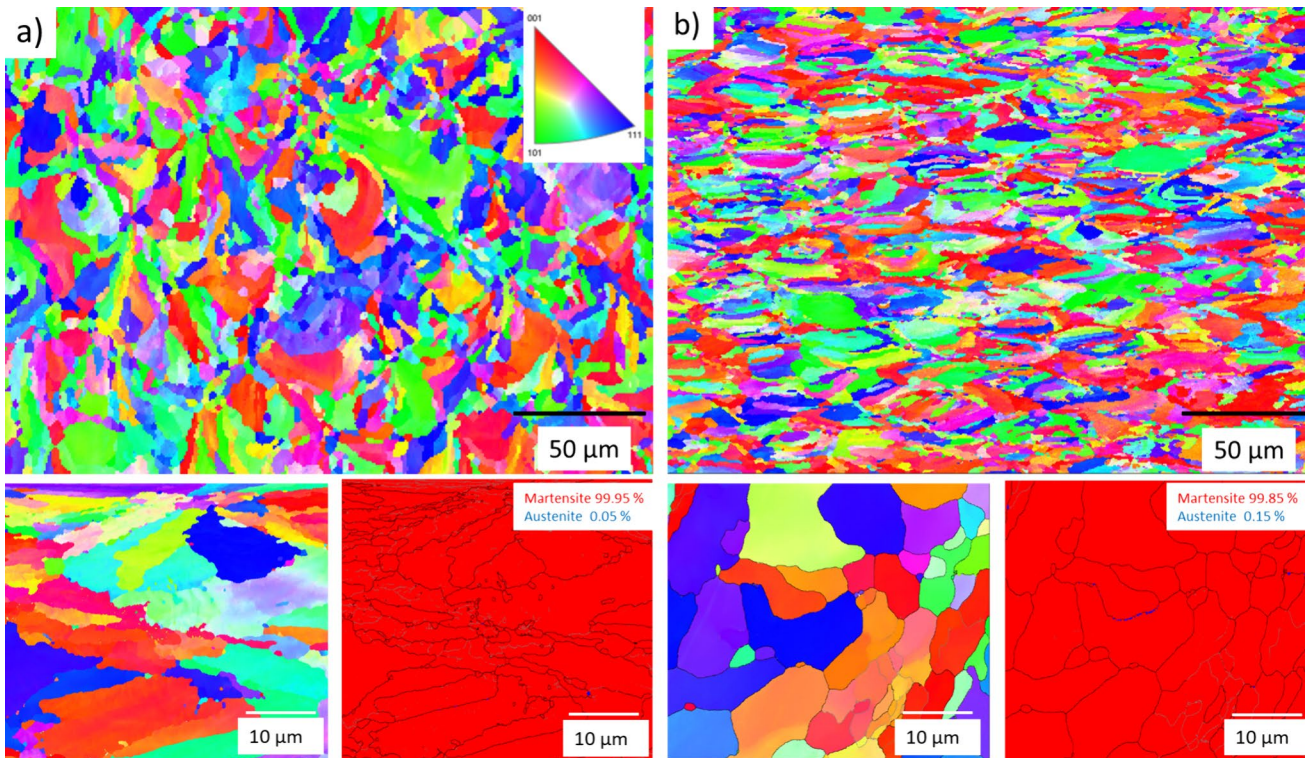

Fig. 8 EBSD orientation maps obtained from L-PBF parts along perpendicular to build direction: (**a**) as-received, (**b**) heat-treated part
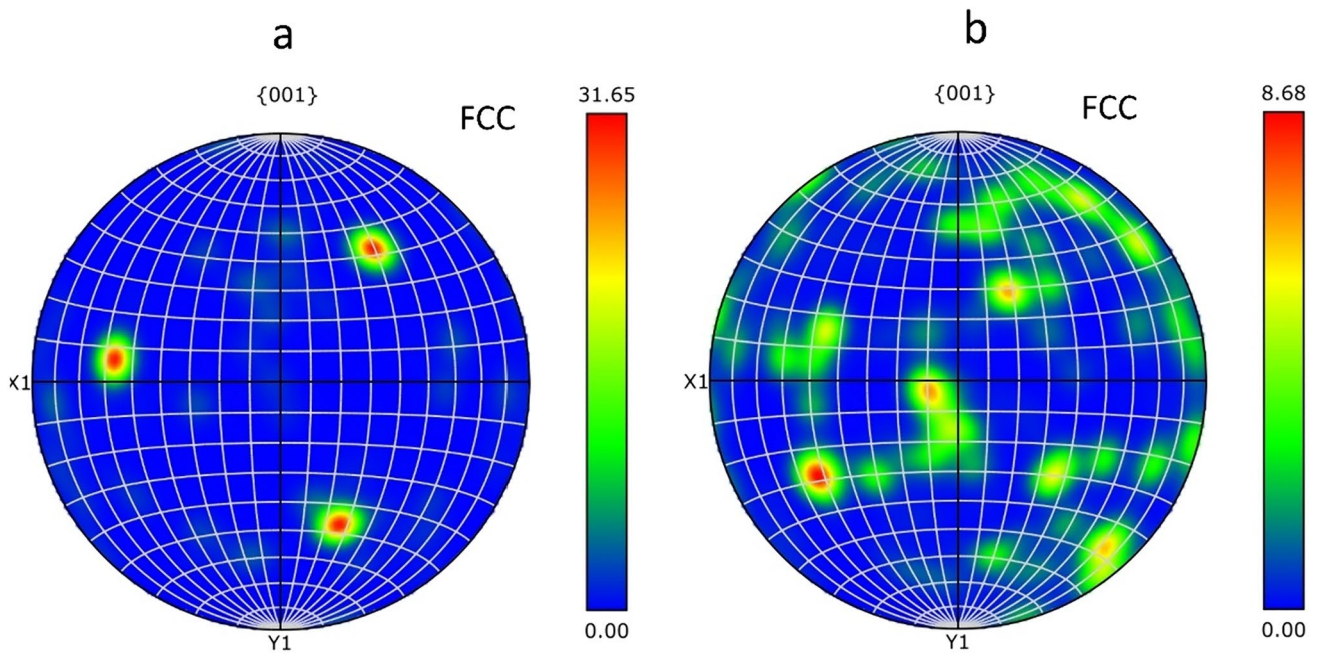
Fig. 9 Pole figure for obtained from L-PBF parts: (**a**) as-received, (**b**) heat-treated part, displaying austenite (FCC) in {100}
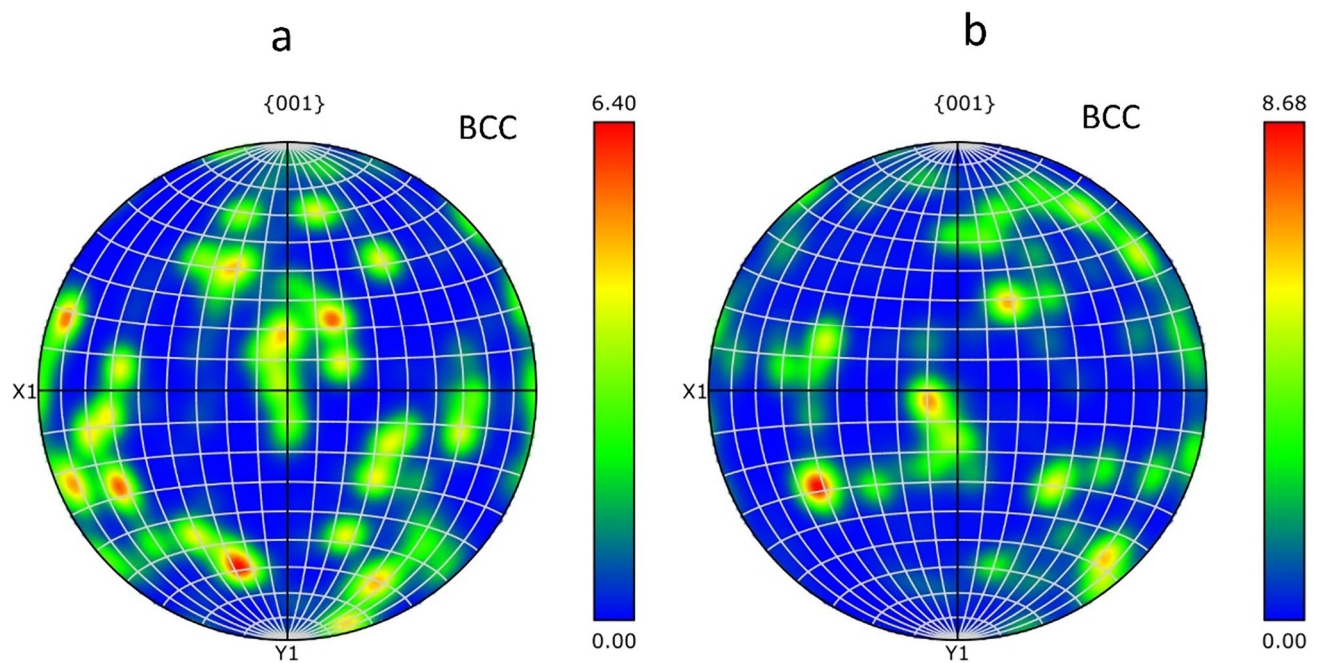

Fig. 10 Pole figure obtained from L-PBF parts: (**a**) as-received, (**b**) heat-treated part, displaying martensite (BCC) in {100}

itself can be seen from the slight increase in the austenite phase and formation of finer grain distribution [51, 54, 55]. Though, the volume fraction of retained austenite in wrought and L-PBF parts are observed to be less than 1%, the resulting austenite grains are really small which reduces the overall grain-size distribution in the microstructure. In addition, the increase in the number of precipitates as observed in Fig. 6 while comparing the microstructure of as-built and heat-treated samples is usually accompanied after heat treatments [54, 55].

3.3 Fracture analysis

Figures 11–12 show SEM images of the fracture surface morphology for the heat-treated and non-heat-treated specimens. A lot of small size dimples in wrought specimens, see Fig. 11, with and without annealed + aging, indicate a plastic deformation occurred during the tensile test. The presence of equiaxed microvoids indicates that the fracture mode is predominantly ductile in nature. In contrast to the wrought specimens, which exhibited a relatively homogeneous microstructure with few imperfections, the L-PBF samples displayed a heterogeneous microstructure with a large number of imperfections of varying sizes, due to defects related to AM process like pores and unmelted powders (see Fig. 12a).

To determine porosity in L-PBF part, its relative density was determined using the Archimedes method in accordance with ASTM B962-14 [56]. The results were compared to the relative density of wrought parts. The density of L-PBF and wrought parts was determined experimentally by measuring
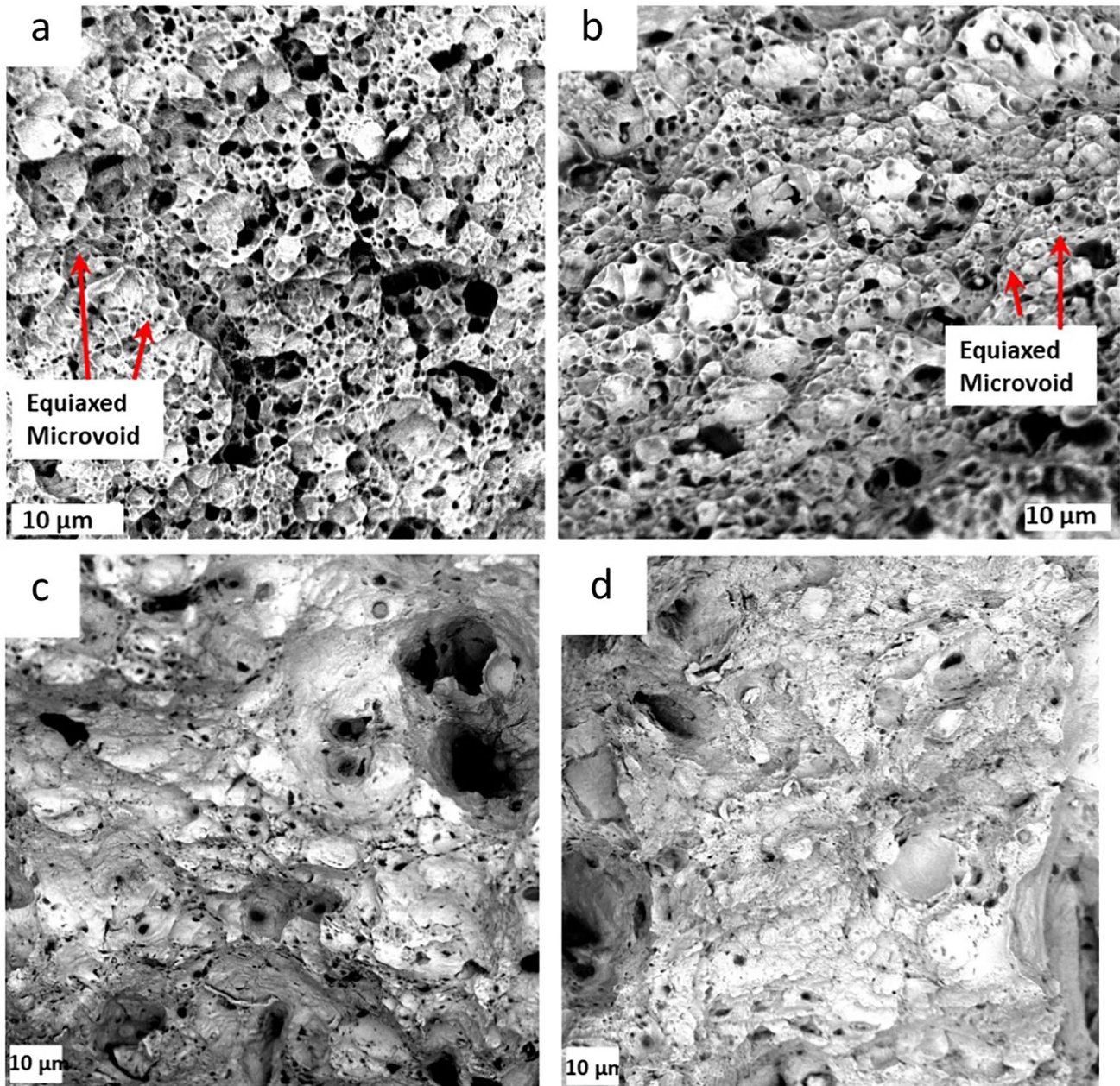

Fig. 11 SEM images illustrating fracture morphologies of (**a**) wrought specimen without heat treatment, (**b**) wrought specimen with heat treatment, (**c**) SLM specimen without heat treatment, **d**. SLM specimen with heat treatment
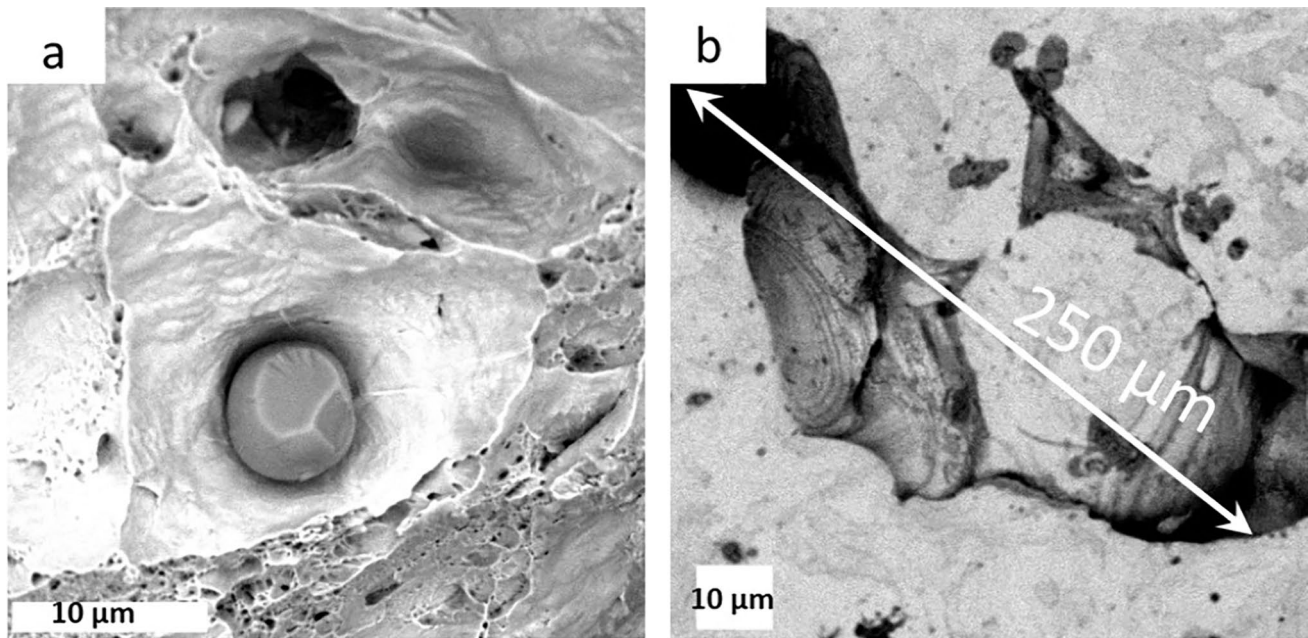
Fig. 12 SEM images showing a lot of unmelted powder (**a**) and pores (**b**), within L-PBF parts produced by ORLAS Creator machine. Solution annealing + aging treatment does not affect unmelted powder in L-PBF part

their mass and volume. The mass of a part was determined by weighing it in air, and the volume was determined by immersing the part in water and measuring the volume of water displaced. The density of the L-PBF parts was 7.57 g/cm^3, while the density of the wrought parts was 7.80 g/cm^3. The relative density of the L-PBF parts was calculated by dividing the density of L-PBF parts over that of wrought parts, which was found to be 97%. This indicates that the L-PBF parts have a lower density than the wrought parts due to the presence of porosity, that can be caused by lack of fusion and entrapped gas. These defects are inherent to the layering process used in AM. The L-PBF machine's scanning precision and powder size distribution may also contribute to part imperfections. The big dimple and unmelted powder shown in Fig. 12b, reveals that the crack may be propagated from the defect areas.

3.4 Micro vickers hardness

The microhardness analysis was conducted employing a Vickers hardness indenter (manufactured by Buehler Inc.). A consistent load of 500 gf, accompanied by a dwell duration of 10 s, was applied at five distinct sites. The resultant microhardness values were subsequently averaged to derive the representative microhardness measurement. The result of the comparative investigation is shown in Fig. 13. The plot shows that the microhardness of wrought and L-PBF specimens increased from 366 to 381 HV and

from 280 to 340 HV, respectively, after heat treatment. A higher hardness after heat treatment is attributed to the finer microstructure with smaller grain-size distribution and the presence of the precipitates such as NbCr$_2$ rich phases or possibility of Cu-rich precipitates, which were confirmed by previous studies [6, 25, 33, 50–52]. The precipitated particles and their associated strain fields act as obstacles to the movement of dislocations which creates additional resistance, thereby increasing the strength and hardness of the alloys. Furthermore, the results of finer microstructure after heat treatment and subsequent reduction of grain-size distribution also acts as obstacles for the dislocations which results in the increase in hardness and strength of the alloy. According to the Hall–Petch relationship, as the grain size decreases the strength and hardness of the material increases. With smaller grain size and finer distribution, the grain boundaries in the refined microstructure further hinders the movement of the dislocation and plastic deformation becomes more challenging which correlates with increase in strength and hardness of a material [51, 54, 55]. It is noteworthy that the increase in microhardness for heat-treated L-PBF specimens was greater than that of wrought specimens. This increase is attributed to grain-size reduction, as the L-PBF parts in the heat-treated condition experienced overall greater average grain-size reduction than the wrought specimens, see Figs. 7 and 8 [57, 58].

Fig. 13 A comparative investigation of micro hardness between parts in as-built and heat-treated conditions
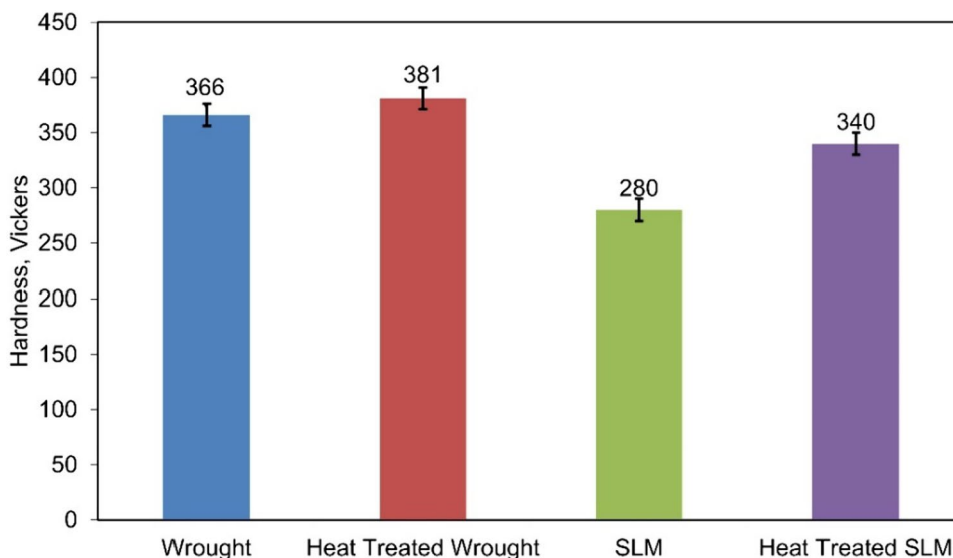

3.5 Nanoindentation tests

The nanoindentation test results, which were used to investigate the nanoscale mechanical properties of both wrought and L-PBF samples, are presented in Figs. 14, 15, 16, 17 and 18. Force–displacement (F-D) profiles were acquired through the implementation of 100 indentations, carried out within a 10×10 grid arrangement, with inter-indentation intervals of 10 µm for every individual specimen. The comparative investigation of these curves reveals that much smaller displacement variations are observed in wrought specimens compared with L-PBF specimens, see Fig. 14. The average indentation depths for L-PBF samples were 250 nm and 180 nm, while those for wrought samples were 240 nm and 220 nm, respectively.

Figures 15, 16 show distribution of nanohardness and reduced modulus elasticity in wrought and L-PBF specimens, respectively. Figures 17, 18 show average nanohardness and reduced elastic of modulus, respectively. Subsequent to heat treatment, both the hardness and modulus of the wrought and L-PBF specimens exhibited an increase, attributed to the presence of precipitates and finer microstructure with smaller grain-size distribution. [20, 51, 54, 55, 59, 60]. Figure 15(a) shows that the as-received wrought parts contain a uniform hardness distribution centered around 5 GPa. Following heat treatment, specific regions within this uniform distribution are distinguished

Fig. 14 Representative force–displacement curves for L-PBF and wrought specimens before and after heat treatment
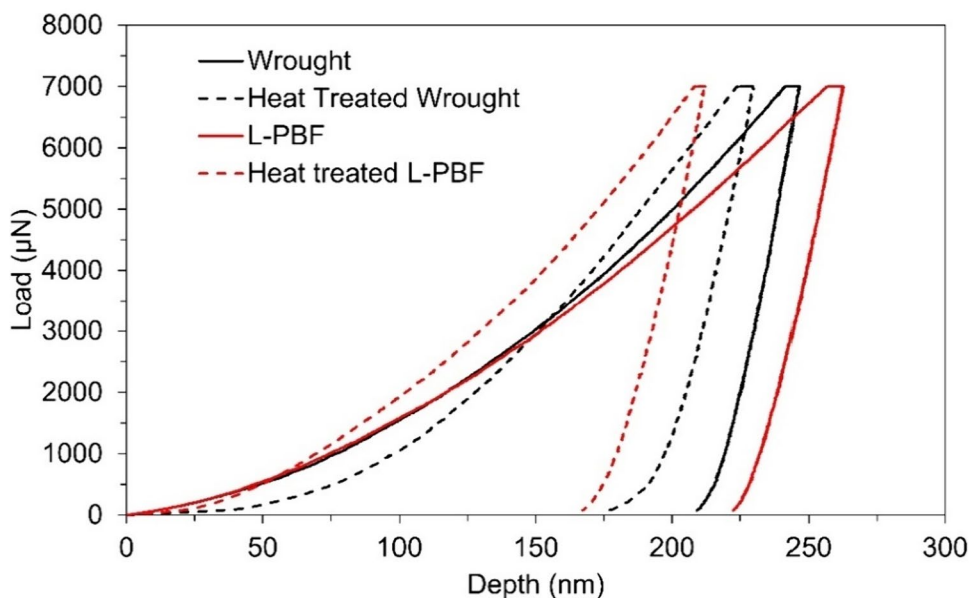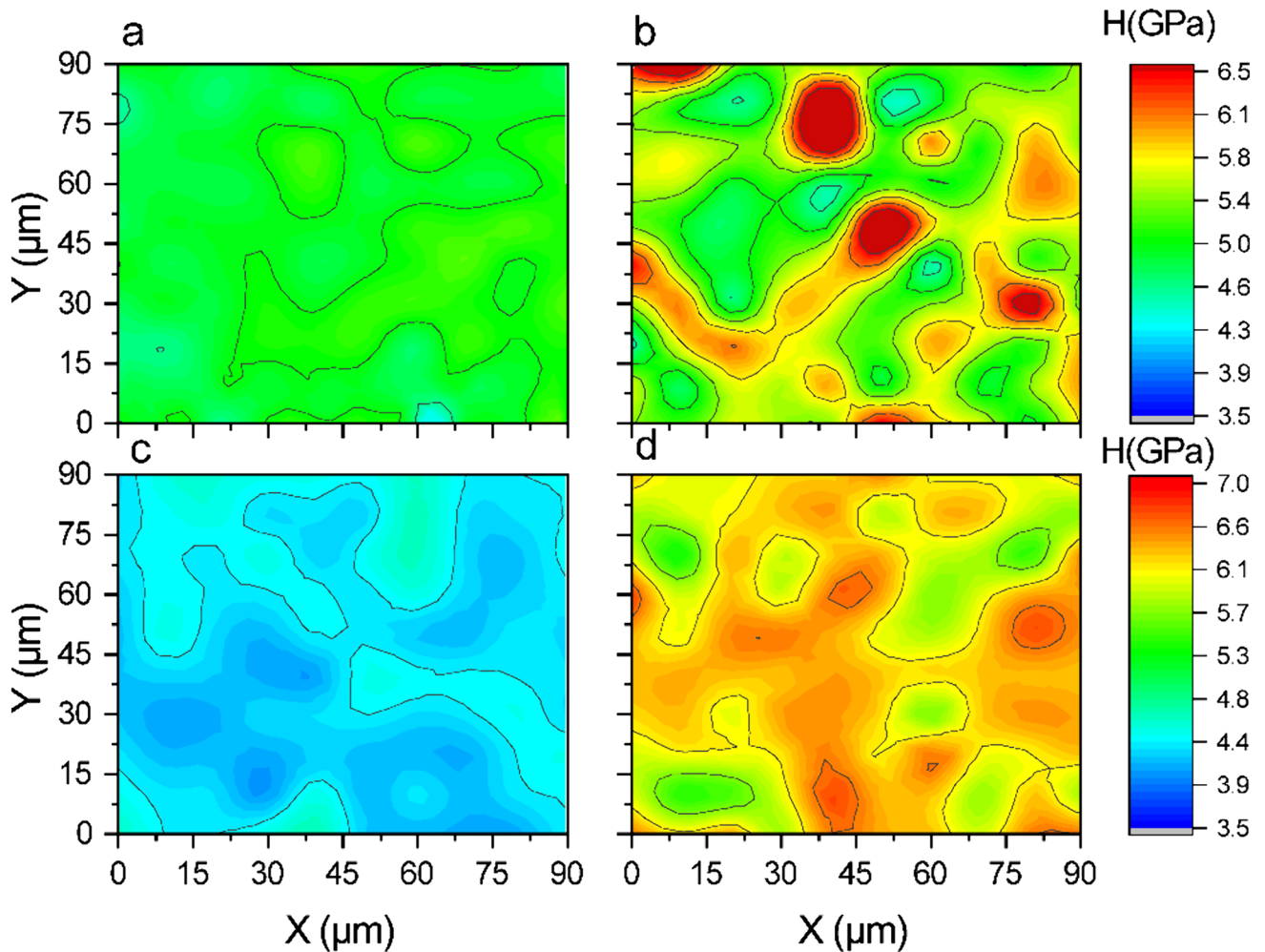
Fig. 15 Surface hardness mapping of wrought and L-PBF specimens, (**a**) as-received wrought, (**b**) heat-treated wrought, (**c**) as-built L-PBF, (**d**) heat-treated L-PBF. The indentation for **c** and **d** were parallel to the printing direction

by elevated hardness values, measuring approximately 6.5 GPa, see Fig. 15(b).

When evaluating reduced modulus of parts, see Fig. 16, it was observed that wrought specimens in heat-treated condition experienced highest values, varying between 188 and 220 GPa. The reduced modulus and nanohardness of parts are correlated, but the level of responsiveness to heat treatment is different. For example, the nanohardness of L-PBF parts increased by 37% after heat treatment, but the reduced modulus only increased by 9%. This difference in responsiveness to heat treatment is likely due to the different mechanisms by which the two properties are affected by heat treatment. In general, hardness is more responsive to changes in microstructure than reduced modulus because it is a more direct measure of the resistance of a material to dislocation motion [61–64]. When a material is deformed, dislocations move through the crystal lattice. The more difficult it is for dislocations to move, the harder the material will

be. Reduced modulus, on the other hand, is not as directly affected by dislocation motion. Modulus is a measure of the elastic properties of a material, which are the properties that govern how a material deforms when it is subjected to a load. The elastic properties of a material are determined by the interatomic forces between the atoms in the material [65]. These forces are not as sensitive to changes in microstructure as the resistance of a material to dislocation motion.

4 Conclusion

In this study, 17-4 PH steel was fabricated by both conventional and additive manufacturing techniques. A comprehensive comparative analysis of the macro, micro, and nano-scale properties between laser powder bed fusion (L-PBF) and wrought parts was conducted. Furthermore, heat
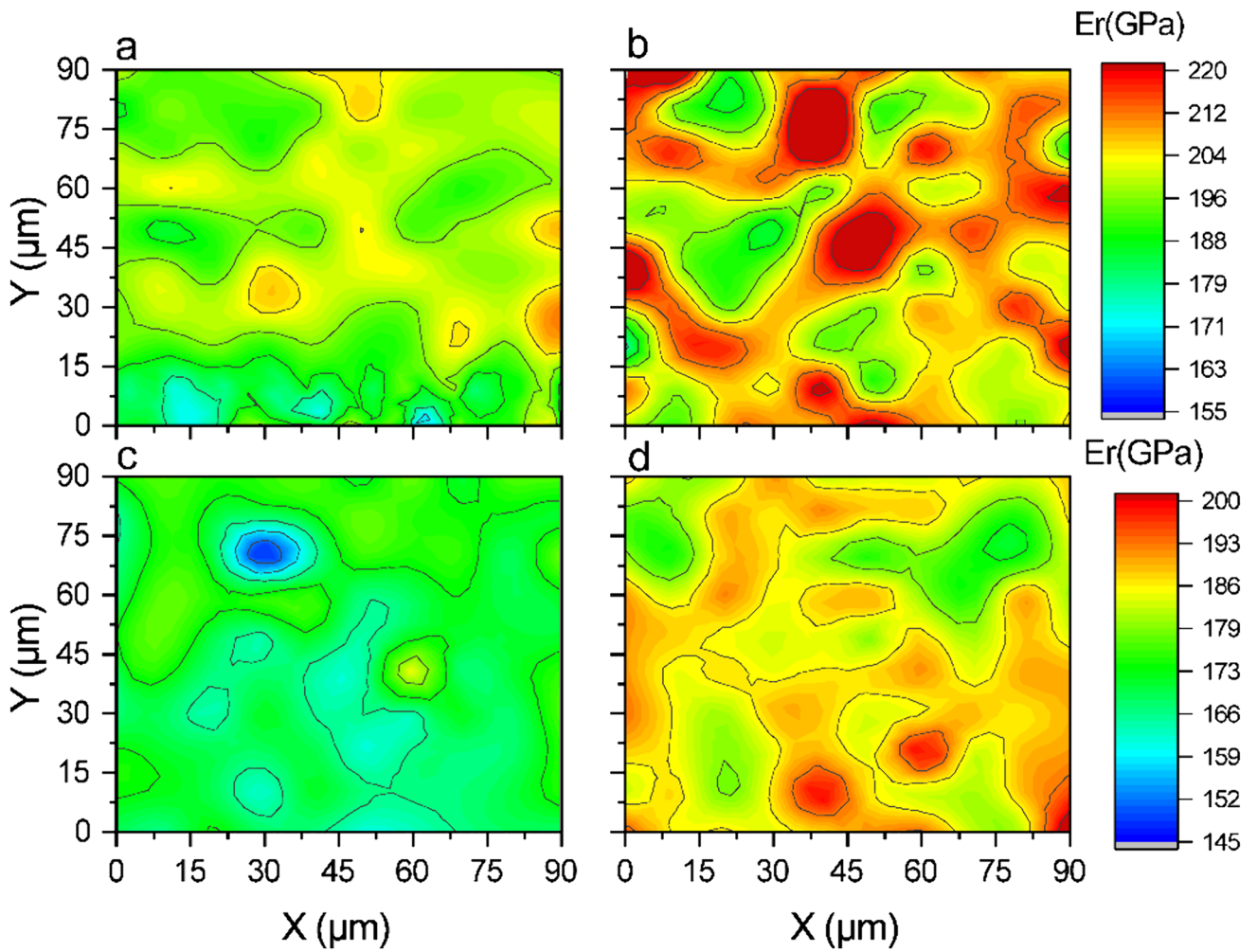
Fig. 16 Surface-reduced modulus mapping of wrought and L-PBF specimens. (**a**) as-received wrought, (**b**) heat-treated wrought, (**c**) as-built L-PBF, (**d**) heat-treated L-PBF. The indentation for **c** and **d** were parallel to the printing direction

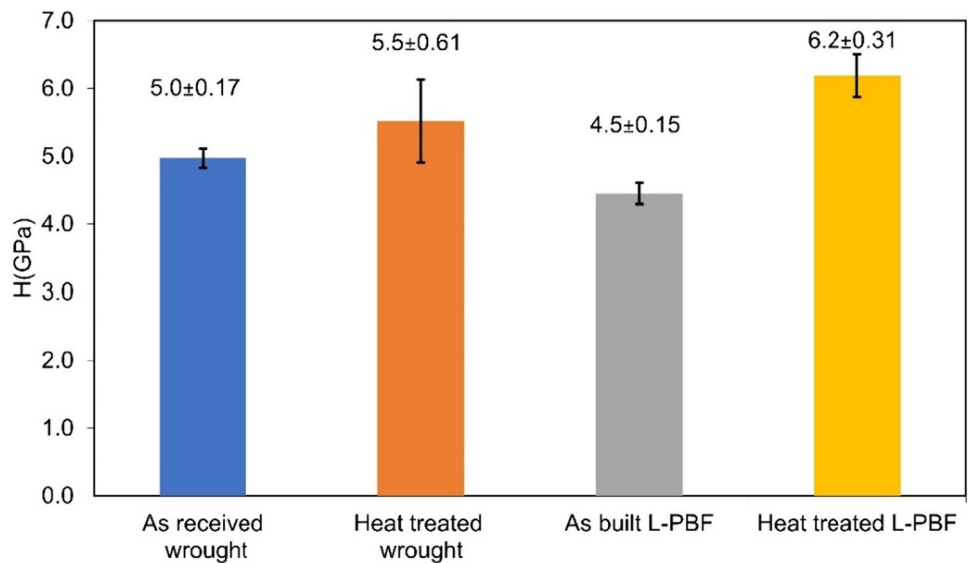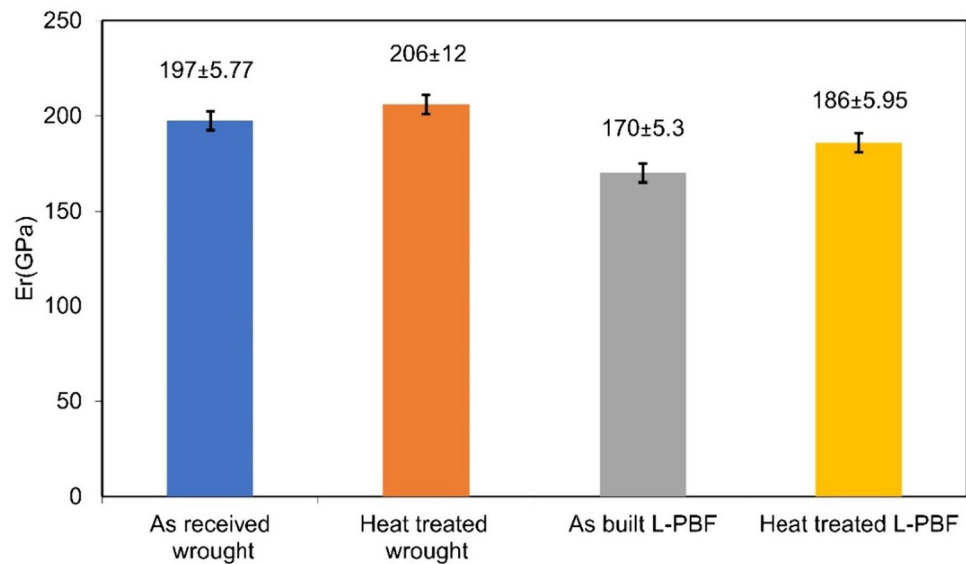**Fig. 17** Average hardness of wrought and L-PBF specimens

Fig. 18 Average reduced modulus of wrought and L-PBF specimens

treatment process was employed to understand its impact on the performance of both L-PBF and wrought samples. The main outcomes are summarized as follows:

1) The microstructure of the 17-4 PH steel showed the presence of martensite and austenite along with a trace amount of NbCr2 precipitates. Both wrought and L-PBF samples present predominantly martensitic microstructures with minimal austenite and resulting in a slight increase in austenite concentration after heat treatment. However, the grain-size distribution exhibited an inverse trend with heat treatment, with an approximate 32% decrease in average grain size for wrought samples and a 29% decrease for L-PBF samples.

2) Heat treatment, through solution annealing + aging, led to increase in yield stress and tensile stress for both L-PBF and wrought specimens, attributed to finer grains and the presence of precipitates in the microstructure. However, ductility decreased for both samples, with the reduction becoming more apparent for the L-PBF sample following the aging step.

3) Both ductility and ultimate strength of L-PBF 17-4 parts were found to be inferior to their wrought parts. This is due to the anisotropy caused by the additive layering approach and the presence of pores, unmelted powder, and precipitates in the microstructure.

4) The increase in microhardness after heat treatment is attributed to a finer microstructure with a reduced-grain-size distribution and the presence of precipitates like NbCr2 rich. These precipitated particles act as obstacles to dislocation movement, enhancing resistance and thereby improving the alloy's strength and hardness.

5) The nano hardness and reduced modulus for both L-PBF and the wrought sample showed a similar tendency to increase after heat treatment. Nanohardness increased by approx. 10% and 38% after treatment for wrought and L-PBF samples, respectively, while reduced modulus rose by approx. 4% and 9%, respectively. This divergence is attributed to dissimilar mechanisms influencing properties response to heat treatment, with hardness more sensitive to microstructural changes. The highest value of hardness was recorded for the treated L-PBF sample with 6.2 ± 0.31 GPa and the lowest being for a cast wrought specimen with 5.0 ± 0.17 GPa.

Declarations

References

1. Huang Y, Leu MC, Mazumder J, Donmez A (2015) Additive manufacturing: current state, future potential, gaps and needs, and recommendations. J Manuf Sci Eng 137:014001. https://doi.org/10.1115/1.4028725

2. Wu M-W, Lai P-H, Chen J-K (2016) Anisotropy in the impact toughness of selective laser melted Ti–6Al–4V alloy. Mater Sci Eng A 650:295–299

3. Frazier WE (2014) Metal additive manufacturing: a review. J Mater Eng Perform 23:1917–1928

4. Du Plessis A, Yadroitsava I, Yadroitsev I (2020) Effects of defects on mechanical properties in metal additive manufacturing: a review focusing on X-ray tomography insights. Mater Des 187:108385

5. Sames WJ, List FA, Pannala S, Dehoff RR, Babu SS (2016) The metallurgy and processing science of metal additive manufacturing. Int Mater Rev 61:315–360. https://doi.org/10.1080/09506608.2015.1116649

6. Yeli G, Auger MA, Wilford K, Smith GDW, Bagot PAJ, Moody MP (2017) Sequential nucleation of phases in a 17-4PH steel: Microstructural characterisation and mechanical properties. Acta Mater 125:38–49. https://doi.org/10.1016/j.actamat.2016.11.052

7. Munther M, Palma T, Tavangarian F, Beheshti A, Davami K (2020) Nanomechanical properties of additively and traditionally manufactured nickel-chromium-based superalloys through instrumented nanoindentation. Manuf Lett 23:39–43. https://doi.org/10.1016/j.mfglet.2019.09.003

8. Carter LN, Martin C, Withers PJ, Attallah MM (2014) The influence of the laser scan strategy on grain structure and cracking behaviour in SLM powder-bed fabricated nickel superalloy. J Alloys Compd 615:338–347. https://doi.org/10.1016/j.jallcom.2014.06.172

9. Parry L, Ashcroft IA, Wildman RD (2016) Understanding the effect of laser scan strategy on residual stress in selective laser melting through thermo-mechanical simulation. Addit Manuf 12:1–15. https://doi.org/10.1016/j.addma.2016.05.014

10. Yusuf SM, Gao N (2017) Influence of energy density on metallurgy and properties in metal additive manufacturing. Mater Sci Technol 33:1269–1289. https://doi.org/10.1080/02670836.2017.1289444

11. Cherry JA, Davies HM, Mehmood S, Lavery NP, Brown SGR, Sienz J (2015) Investigation into the effect of process parameters on microstructural and physical properties of 316L stainless steel parts by selective laser melting. Int J Adv Manuf Technol 76:869–879. https://doi.org/10.1007/s00170-014-6297-2

12. Burkhardt C, Wendler M, Lehnert R, Hauser M, Clausnitzer P, Volkova O, Biermann H, Weidner A (2023) Fine-grained microstructure without texture obtained by electron beam powder bed fusion for AISI 304 L-based stainless steel. Addit Manuf 69:103539. https://doi.org/10.1016/j.addma.2023.103539

13. Gu D, Shen Y (2009) Balling phenomena in direct laser sintering of stainless steel powder: metallurgical mechanisms and control methods. Mater Des 30:2903–2910. https://doi.org/10.1016/j.matdes.2009.01.013

14. Thijs L, Sistiaga MLM, Wauthle R, Xie Q, Kruth J-P, Van Humbeeck J (2013) Strong morphological and crystallographic texture and resulting yield strength anisotropy in selective laser melted tantalum. Acta Mater 61(12):4657–4668. https://doi.org/10.1016/j.actamat.2013.04.036

15. Dadbakhsh S, Vrancken B, Kruth J-P, Luyten J, Van Humbeeck J (2016) Texture and anisotropy in selective laser melting of NiTi alloy. Mater Sci Eng A 650:225–232. https://doi.org/10.1016/j.msea.2015.10.032

16. Sercombe T, Jones N, Day R, Kop A (2008) Heat treatment of Ti-6Al-7Nb components produced by selective laser melting. Rapid Prototyp J 14:300–304. https://doi.org/10.1108/13552540810907974

17. Salari S, Rahman MS, Polycarpou AA, Beheshti A (2020) Elevated temperature mechanical properties of Inconel 617 surface oxide using nanoindentation. Mater Sci Eng A 788:139539. https://doi.org/10.1016/j.msea.2020.139539

18. Jägle EA, Choi P-P, Van Humbeeck J, Raabe D (2014) Precipitation and austenite reversion behavior of a maraging steel produced by selective laser melting. J Mater Res 29:2072–2079. https://doi.org/10.1557/jmr.2014.204

19. Huber D, Stich P, Fischer A (2022) Heat treatment of 17-4 PH stainless steel produced by binder jet additive manufacturing (BJAM) from N2-atomized powder. Prog Addit Manuf 7:187–199. https://doi.org/10.1007/s40964-021-00224-z

20. Hamlin RJ, DuPont JN (2017) Microstructural evolution and mechanical properties of simulated heat-affected zones in cast precipitation-hardened stainless steels 17-4 and 13–8+ Mo. Metall Mater Trans A 48:246–264

21. Rafi HK, Pal D, Patil N, Starr TL, Stucker BE (2014) Microstructure and mechanical behavior of 17-4 precipitation hardenable steel processed by selective laser melting. J Mater Eng Perform 23:4421–4428. https://doi.org/10.1007/s11665-014-1226-y

22. Casati R, Lemke J, Tuissi A, Vedani M (2016) Aging behaviour and mechanical performance of 18-Ni 300 steel processed by selective laser melting. Metals 6:218. https://doi.org/10.3390/met6090218

23. Wang X, Chou YK (2015) A method to estimate residual stress in metal parts made by selective laser melting, ASME Int. Mech Eng Congr Expo Proc 2A–2015:1–8. https://doi.org/10.1115/IMECE2015-52386

24. Abbas TF, Othman FM, Basil Ali H, Effect of infill Parameter on compression property in FDM Process. Int J Eng Res Appl 2017; 7: 16–19. https://doi.org/10.9790/9622-0710021619.

25. Murr LE, Martinez E, Hernandez J, Collins S, Amato KN, Gaytan SM, Shindo PW (2012) Microstructures and properties of 17-4 PH stainless steel fabricated by selective laser melting. J Mater Res Technol 1:167–177

26. Mutua J, Nakata S, Onda T, Chen Z-C (2018) Optimization of selective laser melting parameters and influence of post heat treatment on microstructure and mechanical properties of maraging steel. Mater Des 139:486–497. https://doi.org/10.1016/j.matdes.2017.11.042

27. Yadollahi A, Shamsaei N, Thompson SM, Elwany A, Bian L (2017) Effects of building orientation and heat treatment on fatigue behavior of selective laser melted 17-4 PH stainless steel. Int J Fatigue 94:218–235

28. Roberts D, Zhang Y, Charit I, Zhang J (2018) A comparative study of microstructure and high-temperature mechanical properties of 15–5 PH stainless steel processed via additive manufacturing and traditional manufacturing. Prog Addit Manuf 3:183–190. https://doi.org/10.1007/s40964-018-0051-5

29. LeBrun T, Nakamoto T, Horikawa K, Kobayashi H (2015) Effect of retained austenite on subsequent thermal processing and resultant mechanical properties of selective laser melted 17-4 PH stainless steel. Mater Des 81:44–53. https://doi.org/10.1016/j.matdes.2015.05.026

30. Kudzal A, McWilliams B, Hofmeister C, Kellogg F, Yu J, Taggart-Scarff J, Liang J (2017) Effect of scan pattern on the microstructure and mechanical properties of Powder Bed Fusion additive manufactured 17-4 stainless steel. Mater Des 133:205–215. https://doi.org/10.1016/j.matdes.2017.07.047

31. Sun Y, Hebert RJ, Aindow M (2018) Effect of heat treatments on microstructural evolution of additively manufactured and wrought 17-4PH stainless steel. Mater Des 156:429–440. https://doi.org/10.1016/j.matdes.2018.07.015

32. Cheruvathur S, Lass EA, Campbell CE (2016) Additive manufacturing of 17-4 PH stainless steel: post-processing heat treatment to achieve uniform reproducible microstructure. JOM 68:930–942. https://doi.org/10.1007/s11837-015-1754-4

33. Bai Y, Yang Y, Wang D, Zhang M (2017) Influence mechanism of parameters process and mechanical properties evolution

mechanism of maraging steel 300 by selective laser melting. Mater Sci Eng A 703:116–123. https://doi.org/10.1016/j.msea.2017.06.033

34. Gong X, Lydon J, Cooper K, Chou K. Microstructural analysis and nanoindentation characterization of Ti-6Al-4V parts from electron beam additive manufacturing, in: Vol. 2A Adv. Manuf., American Society of Mechanical Engineers, 2014: pp. 1–8. https://doi.org/10.1115/IMECE2014-36675.

35. Tillmann W, Dias NFL, Stangier D, Schaak C, Höges S (2022) Heat treatment of binder jet printed 17-4 PH stainless steel for subsequent deposition of tribo-functional diamond-like carbon coatings. Mater Des 213:110304

36. Sabooni S, Chabok A, Feng SC, Blaauw H, Pijper TC, Yang HJ, Pei YT (2021) Laser powder bed fusion of 17-4 PH stainless steel: a comparative study on the effect of heat treatment on the microstructure evolution and mechanical properties. Addit Manuf 46:102176

37. Henry TC, Morales MA, Cole DP, Shumeyko CM, Riddick JC (2021) Mechanical behavior of 17-4 PH stainless steel processed by atomic diffusion additive manufacturing. Int J Adv Manuf Technol 114:2103–2114

38. Khadka S, Bilan HK, Ma T, Yuya PA (2023) Laves phase and equiaxed grains formation in directed energy deposited AlCuFeNiTi high entropy alloy. J Alloys Compd 961:171089. https://doi.org/10.1016/j.jallcom.2023.171089

39. Guennouni N, Barroux A, Grosjean C, Maisonnette D, Nivet E, Andrieu E, Poquillon D, Laffont L, Blanc C (2021) Comparative study of the microstructure between a laser beam melted 17-4PH stainless steel and its conventional counterpart. Mater Sci Eng A 823:141718

40. Sanjeev KC, Nezhadfar PD, Phillips C, Kennedy MS, Shamsaei N, Jackson RL (2019) Tribological behavior of 17-4 PH stainless steel fabricated by traditional manufacturing and laser-based additive manufacturing methods. Wear 440:203100

41. T. Strasser, Comparison of Additively Manufactured and Wrought 17–4 PH Stainless Steels in Ultra Low Cycle Fatigue, University of Arkansas, 2020.

42. EOS, EOS StainlessSteel 17-4PH, 2017.

43. Conde FF, Escobar JD, Oliveira JP, Béreš M, Jardini AL, Bose WW, Avila JA (2019) Effect of thermal cycling and aging stages on the microstructure and bending strength of a selective laser melted 300-grade maraging steel. Mater Sci Eng A 758:192–201. https://doi.org/10.1016/j.msea.2019.03.129

44. Monkova K, Zetkova I, Kučerová L, Zetek M, Monka P, Daňa M (2019) Study of 3D printing direction and effects of heat treatment on mechanical properties of MS1 maraging steel. Arch Appl Mech 89:791–804. https://doi.org/10.1007/s00419-018-1389-3

45. Lin X, Cao Y, Wu X, Yang H, Chen J, Huang W (2012) Microstructure and mechanical properties of laser forming repaired 17-4PH stainless steel. Mater Sci Eng A 553:80–88

46. Tan C, Zhou K, Ma W, Zhang P, Liu M, Kuang T (2017) Microstructural evolution, nanoprecipitation behavior and mechanical properties of selective laser melted high-performance grade 300 maraging steel. Mater Des 134:23–34. https://doi.org/10.1016/j.matdes.2017.08.026

47. Nezhadfar PD, Gradl PR, Shao S, Shamsaei N (2022) Microstructure and deformation behavior of additively manufactured 17-4 stainless steel: laser powder bed fusion vs laser powder directed energy deposition. JOM 74:1136–1148. https://doi.org/10.1007/s11837-021-05032-y

48. Biswas N, Ding JL, Balla VK, Field DP, Bandyopadhyay A (2012) Deformation and fracture behavior of laser processed dense and porous Ti6Al4V alloy under static and dynamic loading. Mater Sci Eng A 549:213–221. https://doi.org/10.1016/j.msea.2012.04.036

49. Wei K, Gao M, Wang Z, Zeng X (2014) Effect of energy input on formability, microstructure and mechanical properties of selective laser melted AZ91D magnesium alloy. Mater Sci Eng A 611:212–222. https://doi.org/10.1016/j.msea.2014.05.092

50. Zai L, Zhang C, Wang Y, Guo W, Wellmann D, Tong X, Tian Y (2020) Laser powder bed fusion of precipitation-hardened martensitic stainless steels: a review. Metals 10(2):255. https://doi.org/10.3390/met10020255

51. Garcia-Cabezon C, Castro-Sastre MA, Fernandez-Abia AI, Rodriguez-Mendez ML, Martin-Pedrosa F (2022) Microstructure–Hardness–Corrosion performance of 17-4 precipitation hardening stainless steels processed by selective laser melting in comparison with commercial alloy. Met Mater Int 28:2652–2667. https://doi.org/10.1007/s12540-021-01155-8

52. Garcia-Cabezon C, Hernández CG, Castro-Sastre MA, Fernandez-Abia AI, Rodriguez-Mendez ML, Martin-Pedrosa F (2023) Heat treatments of 17-4 PH SS processed by SLM to improve its strength and biocompatibility in biomedical applications. J Mater Res Technol 26:3524–3543. https://doi.org/10.1016/j.jmrt.2023.08.104

53. Wu J, Wray PJ, Garcia CI, Hua M, Deardo AJ (2005) Image quality analysis: A new method of characterizing microstructures. ISIJ Int 45:254–262. https://doi.org/10.2355/isijinternational.45.254

54. Viswanathan UK, Nayar PKK, Krishnan R (1989) Kinetics of precipitation in 17-4 PH stainless steel. Mater Sci Technol 5:346–349. https://doi.org/10.1179/mst.1989.5.4.346

55. Mirzadeh H, Najafizadeh A (2009) Aging kinetics of 17-4 PH stainless steel. Mater Chem Phys 116:119–124. https://doi.org/10.1016/j.matchemphys.2009.02.049

56. ASTM International, Standard Test Methods for Density of Compacted or Sintered Powder Metallurgy (PM) Products Using Archimedes' Principle, Astm B962–13. i (2013) 1–7. https://doi.org/10.1520/B0962-17.2.

57. Lim YY, Chaudhri MM (2002) The influence of grain size on the indentation hardness of high-purity copper and aluminium. Philos Mag A 82:2071–2080. https://doi.org/10.1080/01418610208235717

58. Li W, Vittorietti M, Jongbloed G, Sietsma J (2020) The combined influence of grain size distribution and dislocation density on hardness of interstitial free steel. J Mater Sci Technol 45:35–43. https://doi.org/10.1016/j.jmst.2019.11.025

59. Guo D, Kwok CT, Tam LM, Zhang D, Li X (2020) Hardness, microstructure and texture of friction surfaced 17-4PH precipitation hardening stainless steel coatings with and without subsequent aging. Surf Coatings Technol 402:126302

60. Akbari Mousavi SAA, Hoseini Hosein Abad SA (2011) Effects of post weld ageing heat treatments on the microstructure of 17-4PH GTA welded joints. Adv Mater Res 264–265:1300–1305. https://doi.org/10.4028/www.scientific.net/AMR.264-265.1300

61. Triwiyanto A, Hussain P, Ismail MC (2013) Microstructure and nanoindentation characterization of low temperature hybrid treated layer on austenitic stainless steel. IOP Conf Ser Mater Sci Eng 46:012043. https://doi.org/10.1088/1757-899X/46/1/012043

62. Leyland A, Matthews A (2000) On the significance of the H/E ratio in wear control: a nanocomposite coating approach to optimised tribological behaviour. Wear 246:1–11. https://doi.org/10.1016/S0043-1648(00)00488-9

63. Long X, Hu B, Feng Y, Chang C, Li M (2019) Correlation of microstructure and constitutive behaviour of sintered silver particles via nanoindentation. Int J Mech Sci 161–162:105020. https://doi.org/10.1016/j.ijmecsci.2019.105020

64. Tanure L, Bakaeva A, Dubinko A, Terentyev D, Verbeken K (2019) Effect of annealing on microstructure, texture and hardness of ITER-specification tungsten analyzed by EBSD, vickers micro-hardness and nano-indentation techniques. J Nucl Mater 524:191–199. https://doi.org/10.1016/j.jnucmat.2019.07.005

65. Sutton AP (2020) Stress. In: Sutton AP (ed) Physics of Elasticity and Crystal Defects. Oxford University Press, Oxford, pp 9–28. https://doi.org/10.1093/oso/9780198860785.003.0002